Open Dartmouth: Faculty Open Access Articles

12-22-2017

# Development and Evaluation of a Connective Tissue Phantom Model for Subsurface Visualization of Cancers Requiring Wide Local Excision

Kimberly S. Samkoe
*Dartmouth College*

Brent D. Bates
*Dartmouth College*

Niki N. Tselepidakis
*Dartmouth College*

Alisha V. Dsouza
*Dartmouth College*

Jason R. Gunn
*Dartmouth College*

*See next page for additional authors*

Follow this and additional works at: https://digitalcommons.dartmouth.edu/facoa

Part of the Bioimaging and Biomedical Optics Commons

**Authors**

Kimberly S. Samkoe, Brent D. Bates, Niki N. Tselepidakis, Alisha V. Dsouza, Jason R. Gunn, Dipak B. Ramkumar, Keith D. Paulsen, Brian W. Pogue, and Eric R. Henderson

# Development and evaluation of a connective tissue phantom model for subsurface visualization of cancers requiring wide local excision

Kimberley S. Samkoe
Brent D. Bates
Niki N. Tselepidakis
Alisha V. DSouza
Jason R. Gunn
Dipak B. Ramkumar
Keith D. Paulsen
Brian W. Pogue
Eric R. Henderson

# Development and evaluation of a connective tissue phantom model for subsurface visualization of cancers requiring wide local excision

Kimberley S. Samkoe,[a,b,c,*] Brent D. Bates,[b] Niki N. Tselepidakis,[c] Alisha V. DSouza,[c] Jason R. Gunn,[c] Dipak B. Ramkumar,[d] Keith D. Paulsen,[b,c] Brian W. Pogue,[b,c] and Eric R. Henderson[d,e]
[a]Dartmouth-Hitchcock Medical Center, Department of Surgery, Lebanon, New Hampshire, United States
[b]Geisel School of Medicine at Dartmouth, Hanover, New Hampshire, United States
[c]Thayer School of Engineering at Dartmouth, Hanover, New Hampshire, United States
[d]Dartmouth-Hitchcock Medical Center, Department of Orthopaedics, Lebanon, New Hampshire, United States
[e]White River Junction VAMC, White River Junction, Vermont, United States

**Abstract.** Wide local excision (WLE) of tumors with negative margins remains a challenge because surgeons cannot directly visualize the mass. Fluorescence-guided surgery (FGS) may improve surgical accuracy; however, conventional methods with direct surface tumor visualization are not immediately applicable, and properties of tissues surrounding the cancer must be considered. We developed a phantom model for sarcoma resection with the near-infrared fluorophore IRDye 800CW and used it to iteratively define the properties of connective tissues that typically surround sarcoma tumors. We then tested the ability of a blinded surgeon to resect fluorescent tumor-simulating inclusions with ~1-cm margins using predetermined target fluorescence intensities and a Solaris open-air fluorescence imaging system. In connective tissue-simulating phantoms, fluorescence intensity decreased with increasing blood concentration and increased with increasing intralipid concentrations. Fluorescent inclusions could be resolved at ≥1-cm depth in all inclusion concentrations and sizes tested. When inclusion depth was held constant, fluorescence intensity decreased with decreasing volume. Using targeted fluorescence intensities, a blinded surgeon was able to successfully excise inclusions with ~1-cm margins from fat- and muscle-simulating phantoms with inclusion-to-background contrast ratios as low as 2:1. Indirect, subsurface FGS is a promising tool for surgical resection of cancers requiring WLE. © 2017 Society of Photo-Optical Instrumentation Engineers (SPIE) [DOI: 10.1117/1.JBO.22.12.121613]

Keywords: near-infrared fluorescence; image-guided surgery; molecular targeting; indirect visualization; sarcoma; ABY-029.

Paper 170254SSPRR received Apr. 21, 2017; accepted for publication Dec. 1, 2017; published online Dec. 22, 2017.

## 1 Introduction

Surgical resection remains a primary treatment for many types of cancer. However, conventional open, white light-guided surgical techniques are plagued by suboptimal recurrence rates, resulting from residual cancer cells left at the cancer site. Numerous advances for surgical resection have been proposed, one of which is the use of fluorescence guidance to aid in identifying tumor boundaries and residual cancer cells.[1] Fluorescence-guided surgery (FGS) has proven particularly useful in cancers of the brain,[2–5] bladder,[6–8] and head and neck,[9,10] because these cancers are present on the organ surface, and can be viewed directly with administration of fluorescent probes combined with specially equipped surgical microscopes. However, many tumors lie below the surface of the organ and are, therefore, not currently amenable to direct fluorescence visualization.

Many subsurface tumors, such as sarcomas, require tumor excision as a single, complete mass with a zone of normal tissue surrounding the tumor, termed a wide local excision (WLE) with negative margins. The presence of cancer cells at the surface of the excised mass defines a positive margin and is associated with increased recurrence rates and decreased survival rates.[11–14]

Unfortunately, positive margin rates following sarcoma resection with curative intent remain in the range of 22% to 34%.[11–13] WLE of subsurface tumors presents several barriers to conventional direct fluorescence visualization because a margin of normal tissue must be maintained around the mass. Useful application of FGS to sarcomas would provide the surgeon with real-time feedback about tumor location and margin thickness. However, successful implementation of FGS for sarcoma resection will require more sophisticated modeling, taking into consideration the absorption and scattering properties of the investing connective tissues—generally fascia, muscle, and fat—with considerations for tumor size and probe uptake both in the tumor and surrounding tissues.

Numerous fluorescent probes have been utilized for oncologic surgery in an off-label fashion[2–9] or investigated at the preclinical stage;[15–23] however, approval of fluorescent probes is slowed by the high cost of drug development. The introduction of good manufacturing practice (GMP)-produced IRDye 800CW (LI-COR Biosciences, Inc., Lincoln, Nebraska) has renewed drug development for FGS applications.[24–26] One resultant drug is ABY-029, a synthetic anti-epidermal growth factor receptor (EGFR) affibody molecule covalently bound to IRDye 800CW. ABY-029 has several advantages that

---

*Address all correspondence to: Kimberley S. Samkoe, E-mail: kimberley.s.samkoe@dartmouth.edu

make it an excellent candidate for future FGS applications. First, human tissue optical properties in the near-infrared region, including reduced water absorption, scattering, and autofluorescence, allow for deeper sampling volumes and increased fluorescence contrast as compared to other wavelengths. Second, the smaller affibody-based molecule provides better enhancement in peripheral tissues compared to larger antibody-based compounds.[27] Third, the excretion kinetics of ABY-029 is fast, resulting in optimal contrast ratios in the order of hours compared to days as is the case for antibody-based compounds.[28] We have tested ABY-029 rigorously in our laboratory for toxicity,[25] as a single-fluorescent agent in glioma detection[28] and in paired-agent imaging of several EGFR expressing cancers.[29–32] ABY-029 received eIND (#122681) approval status in 2016, and the GMP form of ABY-029 was produced for an ongoing phase-0 clinical trial for recurrent glioma resection (NCT0291925).

ABY-029 is a promising agent for targeting soft tissue sarcomas, which overexpress EGFR in 43% to 78% of cases,[33–37] and the ability of this agent to tag EGFR-positive sarcomas is currently being investigated in a phase-0 clinical trial at our institution (NCT03154411). However, to develop indirect, subsurface visualization methodologies for use in WLE applications, modeling, and validation are required in phantom and animal models. Furthermore, an advanced surgical imaging system must be selected and tested appropriately for detection of the fluorophore. There are several open-field preclinical and United States Food and Drug Administration (FDA)-approved FGS systems capable of imaging near-infrared fluorophores, as discussed thoroughly in our recent review.[38] One of these systems, the SPY-Q (Novadaq, Mississauga, Canada), FDA-approved for indocyanine green imaging, has been used by the Rosenthal group for phase I imaging of cetuximab-IRDye 800CW in head and neck cancer resection.[9,39] A second system, the Solaris by PerkinElmer (Waltham, Massachusetts), has several advantages over the SPY system, including fluorescence background correction that increases instrument sensitivity (~1 nM). The Solaris is not currently FDA-approved but may be a strong candidate for future approval.

In this study, we present foundational work defining early methods for FGS application to cancers requiring WLE using the Solaris fluorescence image-guided surgery system. Here, we compare the depth sensitivity and accuracy of the Solaris with two preclinical systems specifically made by LI-COR Biosciences, Inc. (Lincoln, Nebraska) to image IRDye 800CW—the Pearl Impulse and Odyssey CLx. We pursued two primary aims: (1) to delineate the changes in observed fluorescence of IRDye 800CW in human tissue-simulating phantoms in relation to tumor size, tumor depth, bulk tissue type, and imaging system and (2) to investigate the ability of a surgeon, blinded to the location of a tumor-simulating inclusion and guided only with tumor depth modeling data from aim 1, to excise a fluorescent inclusion with ~1-cm negative margins using the Solaris imaging system.

## 2 Methods

### 2.1 General Preparation of Phantom Components

All inclusions and phantoms were made with 10% w/v gelatin (G2500, Sigma-Aldrich, St. Louis, Missouri). Powder gelatin was mixed with distilled water, heated to ~60°C in a microwave, and stirred vigorously while cooling to ~30°C. Appropriate

**Table 1** Gelatin-based phantom preparation parameters.

| | Phantom properties | | |
| --- | --- | --- | --- |
| Simulated tissue type | Gelatin (%, w/v) | Blood (%, v/v) | Intralipid (%, v/v) |
| Tumor/inclusion | 10 | 1 | 1 |
| Muscle | 10 | 2 | 1 |
| Fat | 10 | 0.5 | 0.75 |

amounts of blood, intralipid, and fluorophore (Table 1) were then added, and the mixtures were poured into suitable molds and cooled in an ice bath. Whole bovine blood (Lampire Biological Laboratories, Inc., Pipersfield, Pennsylvania) was used as an absorbing agent in the physiological range in connective tissues of 0% to 2%, where 1% of blood at 800 nm has an absorption coefficient ($\mu_a$) of 0.0004 mm$^{-1}$ and is equivalent to ~20 $\mu$M total hemoglobin.[40,41] Intralipid (Baxter Healthcare Corporation, Deerfield, Illinois) was used as a scattering agent in the physiologically relevant range of 0.5% to 1%, where 1% of intralipid at 800 nm has a scattering coefficient ($\mu_s'$) of 1.0 mm$^{-1}$.[40,42] All phantoms were stored at 4°C until imaging.

### 2.2 Preparation of Well Phantoms for Screening Bulk Tissue Properties

Five-milliliter volume wells ($4 \times 4$) were created in black Delrin® plastic. A panel of connective tissue-mimicking gelatin phantoms was created, with each well containing 50-nM IRDye 800CW. The rows had varying blood (0.5%, 1%, 2%, and 5% v/v) as an absorbing agent, and the columns had varying intralipid (0.5%, 0.75%, 1%, and 1.5% v/v) as a scattering agent.[40–42] The $4 \times 4$ wells were imaged using the 750-nm channel on the Solaris imaging system. The regions-of-interest (ROIs) were created to encompass the entire well, and the average fluorescence intensity per pixel was determined using the "measure" function in Fiji.[43–45]

### 2.3 Preparation of Wedge Phantoms for Imaging Inclusion Depth

Wedge-shaped phantoms were used to study the effect of tumor and tissue properties on depth of imaging. We created this model in three parts: inclusion, bottom base layer, and upper wedge layer (Fig. 1). The inclusion was made with tumor physical properties (Table 1) reflective of the absorption and scatter in human connective tissue[40–42] and with varying size and fluorescent attributes depending on the particular experiment (Table 2): (1) background tissue properties, (2) inclusion concentration, and (3) inclusion size. Disposable serological pipettes (Corning Inc., Corning, New York) were used to create cylindrical inclusions by coating the inside with vegetable oil and then filling the entire pipette with the gelatin inclusion mixture. Once cooled, the gelatin inclusion was removed by pulling on the cotton filter or pushing out with forced air. The bases were cast as positive molds in clear rectangular containers (70 mm × 125 mm, 300-mL volume). The inclusions were placed into the base by cutting an indentation such that the top of the inclusion was flush with the top surface of the base [Fig. 1(a)]. The wedges
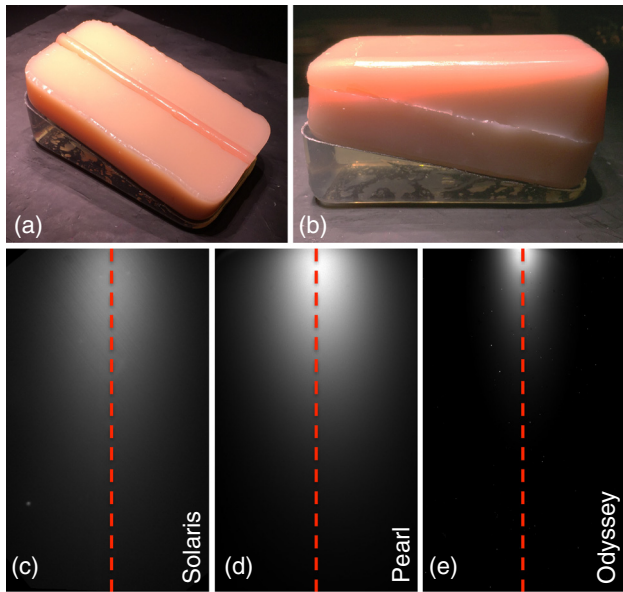
**Fig. 1** Imaging wedge phantoms to determine limits of imaging depth. (a) Bases (2-cm high) with a fluorescent cylindrical inclusion were placed on top of a positioning wedge. (b) A tissue-matched wedge was placed on top, such that the imaging surface was flat. The wedge contained no fluorophore (infinite IBR) or 3:1 IBR. A representative fat, infinite IBR, 8-mm diameter inclusion phantom imaged on the (c) Solaris, (d) Pearl, and (e) Odyssey. The red dashed line indicates the ROI to determine intensity profile of the wedge.

were made in the same rectangular mold but angled such that the inclusion depth varied from 0.5 to 3 cm [Fig. 1(b)]; these were designed to simulate muscle and fat tissues (Table 1).

For imaging on the Solaris (750-nm channel) and Pearl Impulse (800-nm channel), the base and wedge were placed on a clear positioning wedge such that the uppermost surface was a parallel planar surface [Fig. 1(b)]. For imaging on the Odyssey CLx system (800-nm channel), the wedge was placed upside down, such that the imaging surface was flush on the scanning bed, and the base was placed upside down on the wedge. The specifications for each system are noted in Table 3. For each image captured, a straight line ROI was created over top of the inclusion, down the center of the phantom [Figs. 1(c)–1(e)]. The "plot profile" function in Fiji[43–45] was used to create a line profile of fluorescence intensity over the length of the phantom. The length of the phantom was converted to depth in centimeters and plotted against fluorescence intensity. In the inclusion size study (Table 2), the 3:1 inclusion-to-background ratio (IBR) condition did not have a uniform baseline for the control condition (0 mm). Therefore, the fluorescence intensity, $I_{fl}$, of each plot profile in this group was modified to achieve a flat-field corrected (FFC) fluorescence intensity, $I_{fl}(FFC)$, using the following equation:

$$I_{fl}(FCC) = \frac{I_{fl} - I_{fl}(C_\infty)}{I_{fl}(C_{3:1}) - I_{fl}(C_\infty)}, \tag{1}$$

where $I_{fl}(C_\infty)$ and $I_{fl}(C_{3:1})$ are the fluorescence intensities from the no inclusion control conditions of the infinite and 3:1

**Table 2** Experimental phantom parameters for imaging depth in wedge phantoms.

| Experimental variable | Inclusion parameters | | Base parameters | | Wedge parameters | | |
|---|---|---|---|---|---|---|---|
| | Diameter (mm) | IRDye 800CW (nM) | Blood (%, v/v) | Intralipid (%, v/v) | Blood (%, w/v) | Intralipid (%, w/v) | IRDye 800CW (nM) |
| Background tissue properties | 8 | 50 | Tumor/inclusion | | 0, 0.5, 1, 2 | 0.5, 1 | 0 |
| Inclusion concentration | 8 | 0, 5, 10, 20, 50 | Muscle and fat | | Muscle and fat | | 0 |
| Inclusion size | 0, 4, 6, 8, 13, 17 | 50 | Muscle and fat | | Muscle and fat | | 0, 16.7 |

**Table 3** Imaging system specifications.

| Parameter | Imaging system | | |
|---|---|---|---|
| | PerkinElmer Solaris | LI-COR Pearl Impulse | LI-COR Odyssey CLx |
| Imaging setting | Open-air, broad beam | Black box, broad beam | Black box, flatbed scanner |
| Excitation source | White light | Solid-state diode laser | Solid-state diode laser |
| Excitation wavelength | 743SP | 785 | 785 |
| Emission | 770 to 809 | 820LP | 820LP |
| Dynamic range | 16 bit | 22 bit | 22 bit |
| Focal distance | 75 cm | Not specified (~25 to 30 cm) | 0 to 4 mm |
| Detectors/camera | Fluorescence cCMOS camera | CCD, thermoelectrically cooled | Silicon avalanche photodiode |

contrast wedges. Depth of imaging was determined by linearizing each line profile by taking the natural logarithm of the fluorescence intensity and fitting for the intersection with the nonfluorescent control condition.

### 2.4 Preparation of Surgical Phantoms

Inclusions with 50-nM IRDye 800CW were created by pouring cooled gelatin solution (1% blood and 1% intralipid) into disposable tissue embedding molds (22 mm × 22 mm, Electron Microscopy Sciences, Hatfield, Pennsylvania) with 6-0 silk sutures placed through the center to allow for positioning at a later time. The solution was allowed to cool on ice, and then the molds were frozen and stored at −80°C. Varying concentrations of background IRDye 800CW (0, 5, 10, 16.7, and 25 nM) were added to the fat- or muscle-simulating gelatin solutions, such that the IBRs were ∞, 10∶1, 5∶1, 3∶1, and 2∶1, respectively ($n = 3$ for each ratio). Frozen inclusions were then removed from the molds and tethered via the sutures in large cylindrical polypropylene containers (110-mm diameter, 140-mm height, and 1000-mL volume). In a set of surgical test phantoms, inclusions were placed in the center of the container at ∼10 mm from the bottom. In a separate set of surgical dissection phantoms, the inclusions were placed at random locations and ranging from 10 to 30 mm from the bottom. The liquid phantom solution was then poured into all containers to an approximate height of 60 mm, allowing the liquid to cover ∼30 mm above the top of the inclusion for the surgical test phantoms, and ranging from 10 to 30 mm above the top of the inclusion for the surgical dissection phantoms. The phantom containers were cooled on ice and then stored overnight at 4°C. Phantom parameters are summarized in Table 4.

#### 2.4.1 Surgical test phantom imaging

Imaging was performed on Solaris (PerkinElmer) and Pearl Impulse (LI-COR) imaging systems. The 750- and 800-nm channels were utilized for the Solaris and Pearl, respectively. To determine the effect of volume on observed fluorescence, images of each phantom were captured on both systems, and then ∼5 mm was trimmed from the top surface. This process of imaging and trimming was repeated for three additional times, until ∼20 mm had been removed and ∼10 mm remained above the inclusion. Subsequently, holding the inclusion constant in the center of the phantom (∼10-mm depth to inclusion), the sides of the phantom were trimmed and images captured. Five consecutive trimming-imaging sequences were performed until the phantom was reduced to a cube. Volumes were calculated by subtracting water displacement of the removed gel from the total volume of the phantom. Last, once reduced to a cube, each side of the remaining phantom was imaged. After all of the images were captured, the phantoms were then bisected in the horizontal and vertical planes, and the margins (distance from surface to inclusion) for each side were measured with a manual caliper. An ROI capturing the inclusion was drawn on all images, and average fluorescence values were recorded. The effect of volume on the fluorescence signal was investigated by plotting the average ROI fluorescence intensity against volume with decreasing depth to inclusion and then with decreasing side volume. The targeted fluorescence signal for dissection was determined by plotting the measured margin thickness against the natural logarithm of the recorded fluorescence intensity and fit for a target margin thickness of 10 mm.

#### 2.4.2 Surgical phantom dissection

An orthopaedic surgeon (author E.R.H.) was provided targeted fluorescence values (Table 5) representing the expected fluorescence value 10 mm from the inclusion and, subsequently, performed the dissection blinded to the location and depth of the inclusions [Fig. 2(a)]. Using the Solaris to display fluorescence over the surface of the phantom, the surgeon attempted to locate and remove the inclusion with sufficient margins (10 mm) [Fig. 2(b)]. Fifteen phantom dissections were performed for both fat and muscle tissues ($n = 3$ for each IBR). Surgical cuts were made to the phantom, beginning on the outermost aspects and progressing inward, to decrease the margins to ∼10 mm [Figs. 2(c) and 2(d)]. The stopping criteria included: (1) the expected fluorescence signal was reached within approximate dimensions of 4 cm × 4 cm × 4 cm [Figs. 2(e) and 2(f)] or (2) the exposure of any part of the inclusion by a surgical cut, thus representing a positive margin and failed experiment. Each side of the remaining cuboids was imaged, and the block was bisected in the horizontal and vertical planes. Margin thickness of each phantom was measured by manual caliper, plotted against mean fluorescence for the varying tissue types (fat and muscle) and IBRs (∞, 10∶1, 5∶1, 3∶1, and 2∶1), and compared to the targeted fluorescence values.

## 3 Results

### 3.1 Effect of Bulk Tissue Properties on Observed Fluorescence Signal

The observed fluorescence of IRDye 800CW changes with varying concentrations of absorbing (blood) and scattering (intralipid) agents within the optical range of human connective tissue, namely fat, muscle, and tumor (Fig. 3). The range of

**Table 4** Surgical phantom parameters for margin thickness prediction and blinded dissection.

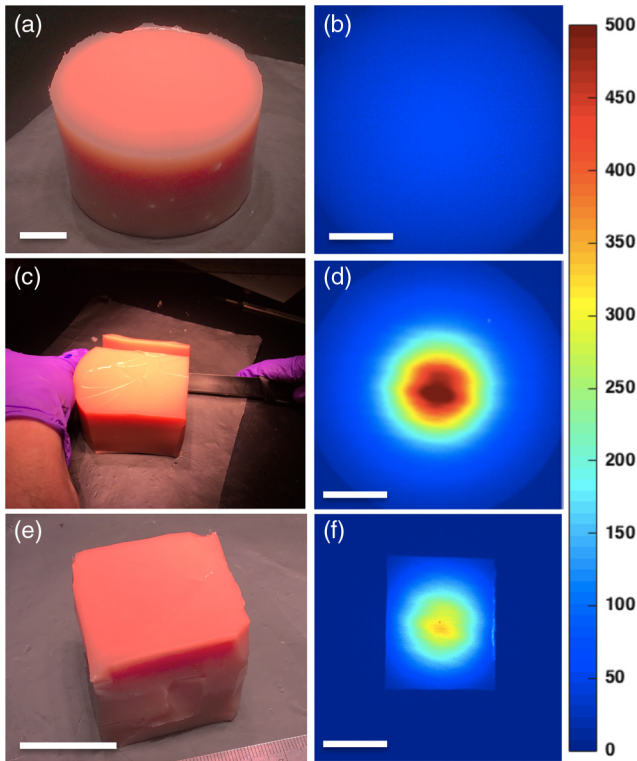| Phantom type | Background | | Inclusion | | |
| | Simulated tissue type | IRDye 800CW (nM) | IRDye 800CW (nM) | Starting depth (mm) | Horizontal location |
|---|---|---|---|---|---|
| Test | Muscle | 0, 5, 10, 16.7, 25 | 50 | 30 | Center |
| | Fat | | | | |
| Dissection | Muscle | 0, 5, 10, 16.7, 25 | 50 | 10, 20, 30 | Random (surgeon blinded) |
| | Fat | | | | |

**Fig. 2** Blinded dissection of fluorescent inclusions (a, c, and e) in white light and (b, d, and f) at 750 nm on the Solaris imaging system. (a and b) Large cylindrical phantoms were created with a 10.6-cm³ inclusion randomly placed in the phantom. (c and d) The surgeon (author E.R.H) used a circular ROI on the Solaris viewing screen to locate the maximal fluorescence intensity and attempt to excise the hidden inclusion. (e and f) The dissection was stopped when the targeted fluorescence reading in the ROI was reached (Table 5) with approximate dimensions of 4 cm × 4 cm × 4 cm. Scale bar = 1 in. in all photos.

phantom conditions representing fat and muscle is indicated in Fig. 3(a), and the specific conditions used throughout this study for fat, muscle, and tumor/inclusion are circled. The fluorescence signal, normalized to the inclusion condition (1% blood and 1% intralipid), was greatest in the 1.5% intralipid and 1.0% blood condition [Fig. 3(b)]. The lowest signal had slightly less than half the signal of the inclusion condition, arising from the 0.5% intralipid and 5.0% blood condition [Fig. 3(b)]. In general, intralipid concentration was proportional to fluorescence, with a plateau observed at the highest concentration (1.5%) [Fig. 3(c)]. In contrast, blood concentration (1.0% to 5.0% range) was inversely proportional to fluorescence signal at all intralipid concentrations, whereas a slight increase in fluorescence was observed from 0.5% to 1.0% blood [Fig. 3(d)].

### 3.2 Effects of Phantom and Inclusion Properties on Depth Sensitivity

The depth of imaging for phantoms with varying background conditions is summarized in Table 6. At 0.5% intralipid, the Solaris and Pearl imaging systems could detect fluorescence emission from the inclusion at >3-cm depth at all blood concentrations; however, the Odyssey had much lower depth sensitivity with a maximum of 2.73 cm observed with 0% blood. At a higher intralipid concentration (1% v/v), the Solaris and Pearl had reduced depth sensitivity; however, both systems could still detect fluorescence at depths >3 cm. In general, the Pearl had greater depth sensitivity compared to the Solaris.

For all imaging systems and phantom properties, as the inclusion concentration increased, depth of imaging also increased (Table 7). The Odyssey demonstrated the lowest depth sensitivity, with the smallest range in depth of imaging among concentrations. The Solaris and the Pearl displayed similar range in depth sensitivity, but in general, the Pearl was more sensitive to a greater depth.

**Table 5** Targeted and actual fluorescent values, and margin thicknesses for fat- and muscle-mimicking surgical phantom dissections.

| | Background IRDye 800CW concentration (nM) | Fluorescence signal (cps) | | | | | Margin thickness (mm) | | | |
| | | Target (Fit) values | | Actual values | | | | Actual thickness | | |
| | | Mean | SD | Mean | SD | Percent error | Target thickness | Mean | SD | Percent error |
|---|---|---|---|---|---|---|---|---|---|---|
| Fat | 0 | 609 | 213 | 923 | 489 | 51.6 | 10 | 9.9 | 2.0 | −0.8 |
| | 5 | 1034 | 446 | 1381 | 434 | 33.6 | 10 | 11.2 | 2.0 | 11.9 |
| | 10 | 2102 | 354 | 1978 | 307 | −5.9 | 10 | 11.0 | 2.9 | 9.6 |
| | 16.7 | 2490 | 89 | 2718 | 158 | 9.1 | 10 | 10.0 | 2.0 | 0.3 |
| | 25 | 3466 | 282 | 4007 | 330 | 15.6 | 10 | 10.6 | 3.7 | 5.7 |
| Muscle | 0 | 334 | 25 | 785 | 401 | 134.9 | 10 | 9.6 | 1.6 | −4.2 |
| | 5 | 950 | 117 | 1247 | 322 | 31.3 | 10 | 9.3 | 1.5 | −7.1 |
| | 10 | 1390 | 41 | 2155 | 457 | 55.1 | 10 | 8.4 | 1.6 | −16.4 |
| | 16.7 | 2046 | 147 | 2507 | 212 | 22.6 | 10 | 9.2 | 2.5 | −7.7 |
| | 25 | 2982 | 388 | 3124 | 317 | 4.8 | 10 | 8.9 | 1.8 | −10.8 |
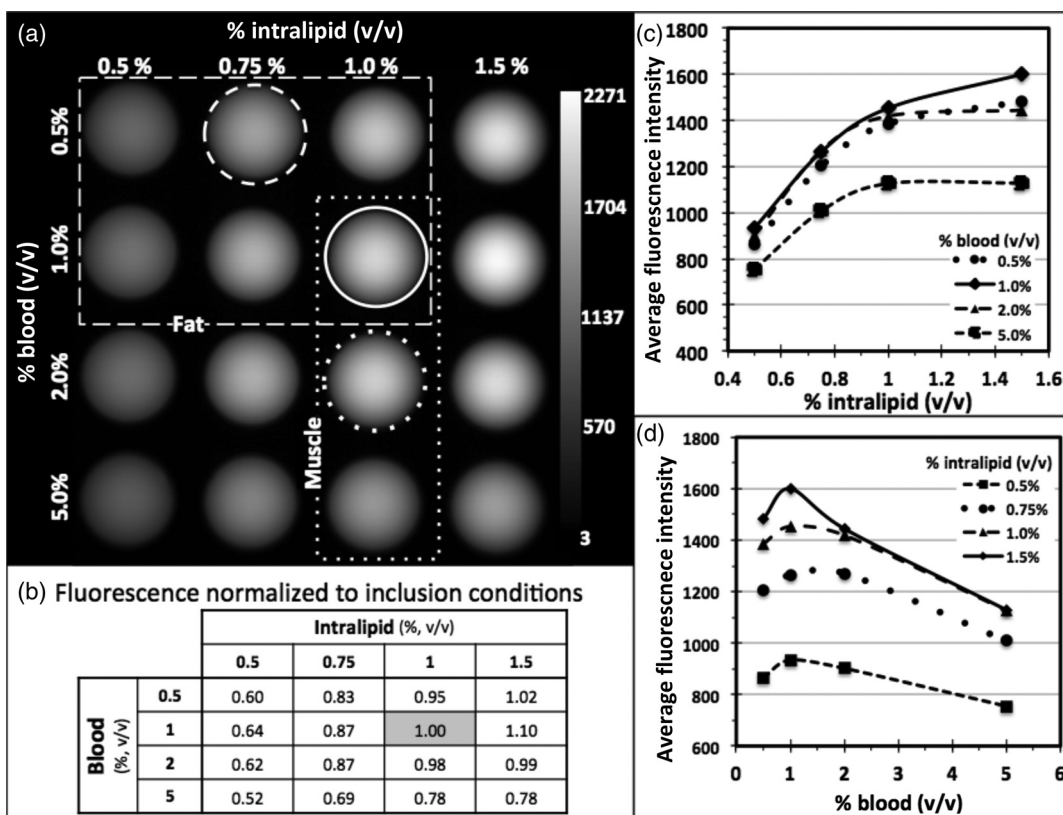
**Fig. 3** Testing the observed fluorescence of IRDye 800CW based on bulk tissue properties of connective tissues relevant to sarcoma. (a) Gelatin well phantoms with constant IRDye 800CW concentration (50 nM) had varying intralipid (columns) and blood (rows) content. The range of properties for fat (dashed) and muscle (dotted) is indicated. The individual circled wells indicate the tissue properties used for fat (dashed), muscle (dotted), and tumor/inclusion (solid) throughout this study. (b) The fluorescence of each condition normalized to the tumor/inclusion fluorescence signal. (c) The effect of varying intralipid concentration on fluorescence signal. (d) The effect of varying blood concentration on fluorescence signal.

Depth of imaging was proportional to inclusion size for the infinite background condition when using the Pearl and Solaris imaging systems; however, the Odyssey demonstrated a relatively constant penetration depth in all cases (Table 8). Graphs demonstrating detection limits of the Pearl using fat

phantoms with infinite and 3:1 IBR can be seen in Fig. 4. For the fat 3:1 IBR, there was a proportional but small increase in depth of imaging for all instruments when the inclusion size was increased. In contrast, imaging depth in the muscle 3:1 IBR condition was inversely proportional to the inclusion size in the Pearl and Solaris; however, the fluorescence plot profiles could not be analyzed for the Odyssey because the natural logarithm of the plot profiles did not intersect with the control case (0 mm) for a positive depth value for each inclusion size. Overall, the Pearl had the highest depth sensitivity, followed by the Solaris, and then the Odyssey (Table 8).

### 3.3 Effects of Tissue Volume on Observed Fluorescence Signal

The surgical "testing" phantoms were used to study the effects of phantom volume on observed fluorescence intensity. In all cases, the ROI was placed in the center of the phantom and measurements were taken after every cut. We observed the same trends for the Solaris and Pearl systems; therefore, the Solaris data are presented in Fig. 5 (Pearl data not shown). Initially, volume was removed from the upper surface of the phantom in ~5-mm increments reducing the height of the phantom [Figs. 5(a)–5(c)]. For both fat and muscle phantoms, the maximum fluorescence intensities recorded for each individual phantom occurred after the final slice was removed (closest to

**Table 6** Effect of background tissue properties on depth of imaging.

| % Intralipid (v/v) | % Blood (v/v) | Depth of imaging (cm) | | |
|---|---|---|---|---|
| | | Solaris | Pearl | Odyssey |
| 0.5 | 0 | 4.05 | 5.02 | 2.73 |
| | 0.5 | 3.73 | 4.71 | 2.64 |
| | 1.0 | 3.49 | 4.15 | 2.58 |
| | 2.0 | 3.31 | 3.82 | 2.47 |
| 1.0 | 0 | 3.80 | 4.17 | 2.66 |
| | 0.5 | 3.53 | 3.67 | 2.47 |
| | 1.0 | 3.35 | 3.43 | 2.38 |
| | 2.0 | 3.18 | 3.11 | 2.12 |

**Table 7** Effect of IRDye 800CW inclusion concentration on depth of imaging. Columns labeled "fat" and "muscle" represent phantoms with fat- and muscle-simulating wedge layers, respectively.

| Inclusion IRDye 800CW (nM) | Depth of imaging (cm) | | | | | |
|---|---|---|---|---|---|---|
| | Solaris | | Pearl | | Odyssey | |
| | Fat | Muscle | Fat | Muscle | Fat | Muscle |
| 5 | 1.86 | 0.98 | 2.77 | 2.42 | 1.53 | 1.35 |
| 10 | 2.01 | 1.94 | 3.20 | 2.51 | 1.66 | 1.51 |
| 20 | 2.29 | 1.94 | 3.52 | 2.64 | 1.67 | 1.48 |
| 50 | 2.51 | 2.23 | 3.72 | 3.02 | 2.07 | 1.56 |

the inclusion), such that fluorescence increased with decreasing volume. As the background fluorescence increased, the overall fluorescence value also increased, such that the 2:1 IBR (25-nM background) phantom had the highest fluorescence, and the infinite IBR (0-nM background) phantom had the lowest fluorescence. These data are demonstrated in the insets of Figs. 5(a) and 5(b) for fat and muscle, respectively. When the fluorescence intensities for each IBR phantoms were normalized to the initial fluorescence reading, each IBR condition displayed a unique curve, dependent on the depth to inclusion (as observed in the wedge phantoms). However, when the depth was held constant and the volume reduced by removing gelatin from the sides of the phantom, normalized fluorescence values decreased in a similar fashion across all conditions, regardless of IBR and observed fluorescence intensity [Figs. 5(d)–5(f)].

### 3.4 Surgical Phantom Dissection

The surgical testing phantoms with known inclusion location were used to calculate target fluorescence values approximating a margin thickness of 10 mm (Table 5). These values were applied in a secondary study where the surgeon was blinded to the location of the inclusion and used only the average fluorescence value across the surface of the phantom to localize and

dissect the inclusion with a goal of 10-mm margins. The surgeon was able to successfully dissect all surgical phantoms from infinite to 2:1 IBR without cutting into the inclusion. In all cases, the surgeon was able to dissect close to the 10-mm margin limit based solely on the provided fluorescence signals obtained from the testing phantoms (Table 5 and Fig. 6). In general, the margins on the fat phantoms were slightly larger than 10 mm but had more spread in the data points, whereas the margins obtained on the muscle phantoms were slightly lower than 10 mm and grouped more tightly [Fig. 6(a)]. The average margin fluorescence increased with increasing background fluorescence and was generally higher for fat than it was for muscle [Table 5 and Fig. 6(b)]. Interestingly, the surgical dissection phantoms generally displayed higher fluorescence intensities than the surgical testing phantoms (Table 5).

## 4 Discussion

The excision of sarcoma tumors with clear, negative margins remains a challenge for oncologic surgeons. In light of recent developments in FGS, ABY-029 is being tested as an EGFR-targeted agent capable of providing sufficient fluorescence contrast to perform WLE of sarcoma tumors using indirect fluorescence imaging methods. To test the ability of PerkinElmer's Solaris imaging system for surgical guidance to detect *in vivo* microdose levels of IRDye 800CW—the fluorescent agent covalently bound to the anti-EGFR affibody agent—we compared its imaging capabilities to two commonly used preclinical systems designed specifically for IRDye 800CW—the LI-COR Pearl Impulse and the LI-COR Odyssey CLx. We have an extensive history of using both of these instruments for *in vivo* and *ex vivo* small rodent preclinical imaging studies using ABY-029.[27,28,31,32,46–49] Furthermore, the Odyssey CLx will be used in the clinical trial of ABY-029 in sarcoma resection (NCT03154411) to obtain high-resolution images of resected tissue that could be up to several centimeters thick; thus, comparison of the depth of imaging of these systems is clinically applicable.

The Solaris system is an open-air imaging system capable of imaging in room lighting and has two channels (750 and 800 nm) that are able to image IRDye 800CW. The 750-nm channel (743-nm short pass excitation and 770- to 809-nm

**Table 8** Effect of inclusion diameter on depth of imaging. Columns labeled "fat" and "muscle" represent phantoms with fat- and muscle-simulating wedge layers, respectively. Columns labeled "∞" and "3:1" represent phantoms with ∞ and 3:1 inclusion-to-background contrast ratios, respectively.

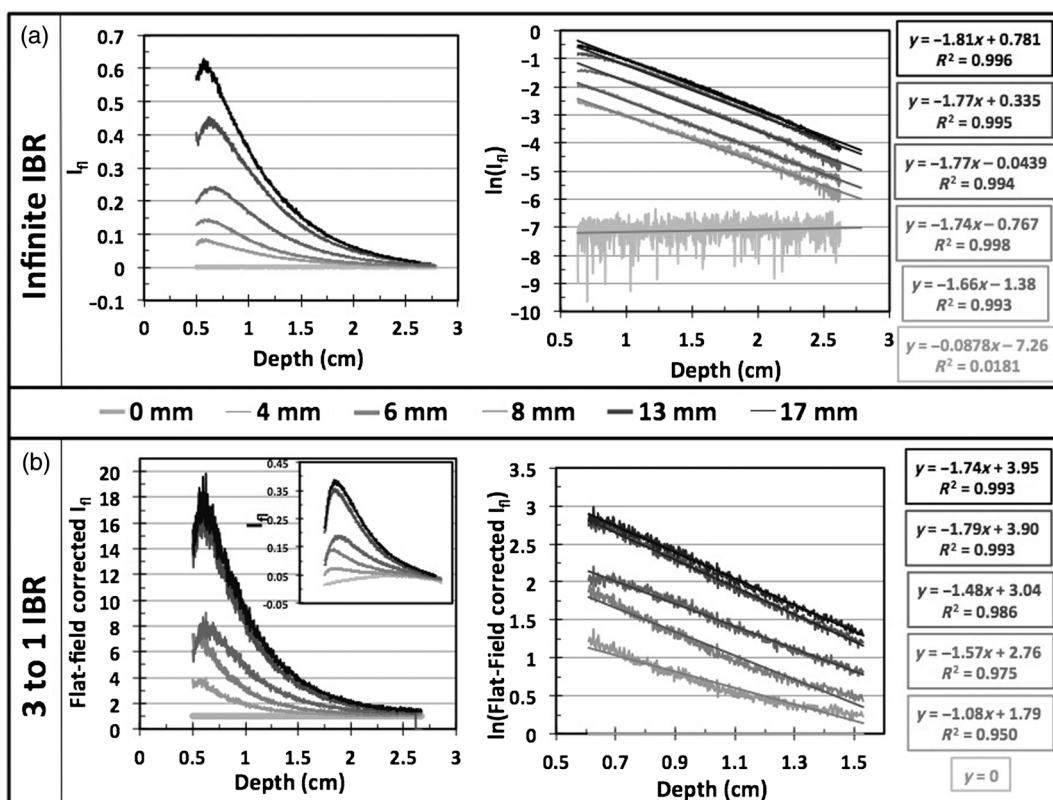| Inclusion diameter (mm) | Depth of imaging (cm) | | | | | | | | | | | |
|---|---|---|---|---|---|---|---|---|---|---|---|---|
| | Solaris | | | | Pearl | | | | Odyssey | | | |
| | Fat | | Muscle | | Fat | | Muscle | | Fat | | Muscle | |
| | ∞ | 3:1 | ∞ | 3:1 | ∞ | 3:1 | ∞ | 3:1 | ∞ | 3:1 | ∞ | 3:1 |
| 4 | 2.60 | 2.34 | 2.02 | 1.71 | 3.55 | 1.66 | 2.32 | 1.57 | 2.89 | 1.54 | 1.15 | — |
| 6 | 2.85 | 2.47 | 2.12 | 1.16 | 3.74 | 1.75 | 2.78 | 1.42 | 2.67 | 1.57 | 1.32 | — |
| 8 | 2.99 | 2.53 | 2.21 | 1.14 | 4.08 | 2.06 | 2.92 | 1.48 | 2.80 | 1.64 | 1.38 | — |
| 13 | 3.21 | 2.70 | 2.33 | 1.13 | 4.29 | 2.18 | 3.06 | 1.38 | 2.89 | 1.72 | 1.43 | — |
| 17 | 3.14 | 2.80 | 2.35 | 1.11 | 4.44 | 2.28 | 2.99 | 1.36 | 2.89 | 1.75 | 1.47 | — |

**Fig. 4** An example of determining detection limits for depth of imaging in fat wedge phantoms with varying inclusion sizes using the Pearl. (a) Infinite IBR: Left—plot profile from each wedge phantom with varying inclusion size and right—the plot profiles are linearized and fit to determine depth of imaging (interception with control condition, 0 mm). (b) 3:1 IBR: Left—the plot profiles are shown as background subtracted, where the background is the control 0-mm condition, and as the raw data (inset) and right— linearized plot profiles of each inclusion size are fit to determine depth of imaging, where resolution limit is when $y = 0$.

emission) is suggested by the manufacturer and produces higher intensity images. Comparatively, the Pearl is a black-box imaging system with optical parameters tailored specifically for IRDye 800CW, including a 785-nm excitation laser and 820-nm detection. The Odyssey is also specifically designed to image IRDye 800CW and contains a 785-nm solid-state diode laser excitation and silicon avalanche photodiode emission detection. The optical components of the Odyssey give it incredible resolution and detection sensitivity with 4 logs of dynamic range in manual mode. This allows the Odyssey to obtain high-resolution, surfaced detailed images that can be compared to histological and immunohistochemical tissue sections. However, the laser beam is focused via microscope on the surface of the imaging plane (or up to 4-mm depth) and, thus, reducing light penetration into tissue and resultant fluorescence collection as compared to wide-field imaging.

As anticipated, in both fat- and muscle-mimicking tissue phantoms, the Pearl outperformed both the Solaris and Odyssey in depth detection of inclusions varying in size and IRDye 800CW concentration. However, despite the decreased performance of the Solaris in imaging depth and sensitivity, performance remained comparable to the Pearl—an achievement likely obtained by proprietary background correction in the Solaris software.[38] Both the Pearl and the Solaris demonstrated higher depth sensitivity than the Odyssey system, especially at lower IRDye 800CW concentrations and inclusion sizes.

Interestingly, the depth of imaging on the Odyssey scanner varied minimally over all conditions, especially in the inclusion size study (Table 8). A similar effect has been observed previously by our group when using a flat bed scanning system to image fluorescent phantoms. In a previous study, we observed no increase in fluorescence on a flat bed scanner when the diameter of a fluorescent inclusion was increased[50] while the broad beam systems displayed a fluorescence increase. This suggests that the flat bed scanning systems are highly surface weighted due to the close proximity of the sample to both the excitation source and detector and, therefore, do not probe the same depth and volume as a broad beam system. However, flat bed scanners offer several advantages, particularly in their reduced susceptibility to fluorescence blooming. While the specifications and uses of the Solaris system differ from those of the Pearl and Odyssey, the Solaris successfully performs as an advanced imaging system adequate for clinical applications.

Connective tissues relevant to sarcoma resection have different optical properties (scattering and absorption),[40] and the Solaris system offers a wide range of imaging capabilities for investigating the differences in these tissues. Nonlinear fluorescent effects occurred at intralipid concentrations >1%, and fluorescence intensity substantially decreased with increasing blood concentration >2%. For this reason, when testing depth sensitivity relative to IRDye 800CW concentration and volume (inclusion size), human muscle properties were selected at
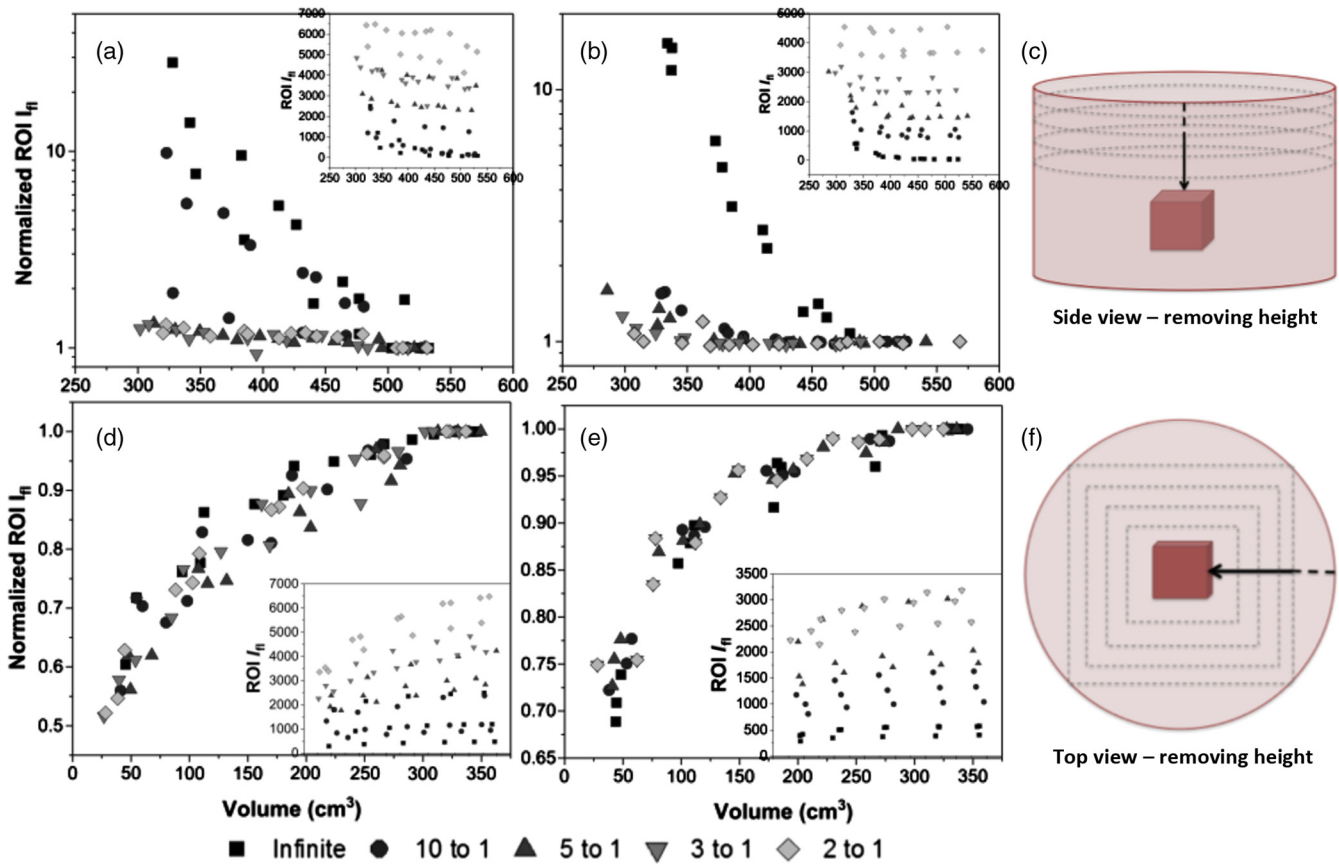
**Fig. 5** Effects of volume on fluorescence intensity of a single ROI within the phantom. The change in fluorescence intensity in (a) fat and (b) muscle phantoms as the height of the phantom is reduced (c) by cutting downward toward the inclusion. Note the y-axis is in log format to visualize all IBR. The change in fluorescence intensity in (d) fat and (e) muscle phantoms as (f) the sides of the phantom are removed while the height of the phantom remains constant. In all cases, the inset shows nonnormalized data to demonstrate the increase in overall intensity as background fluorescence increases (IBR decreases).
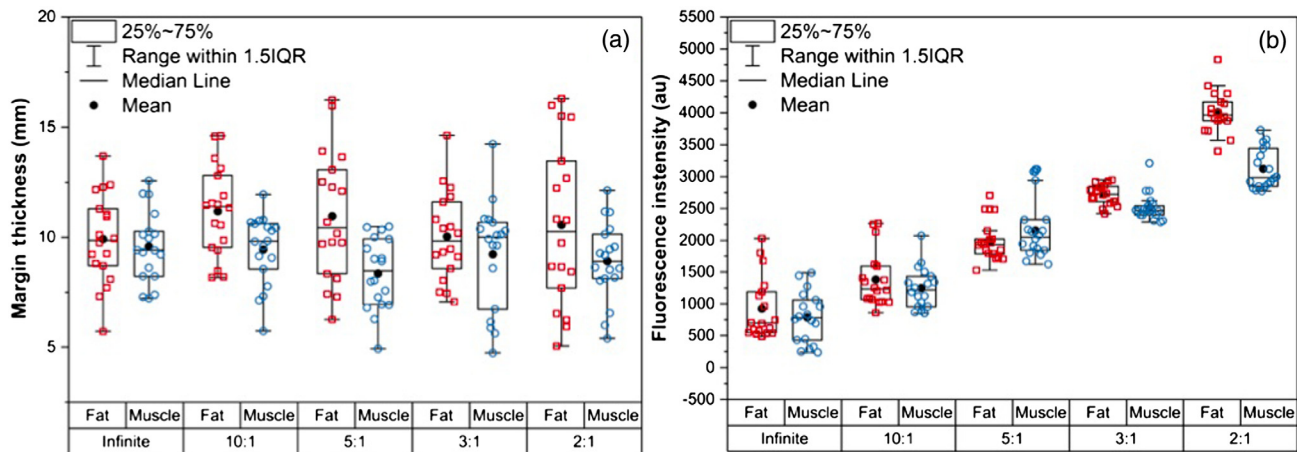


**Fig. 6** Measured (a) margin thickness and (b) fluorescence intensity obtained by blinded surgical dissection of fat and muscle phantoms with increasing IBR.

the lower end range of blood volume.[40–42] The properties chosen for fat were moderate values, with both variables lower than that of the inclusion parameters.[40–42]

In ideal imaging conditions, where the background tissue contained no fluorophore and thus theoretically infinite inclusion contrast, the Solaris, Pearl, and Odyssey were able to resolve fluorescent inclusions deeper than 1 cm at all inclusion sizes and IRDye 800CW concentrations, with the single exception of the Solaris when imaging muscle phantoms containing the lowest concentration inclusions (5 nM). However, when background fluorescence concentrations were increased to achieve 3 : 1 IBR, depth penetration in all systems was greatly

reduced. In fact, in all cases, it was difficult to distinguish among the various inclusion sizes and depth sensitivity in the muscle 3:1 IBR condition tested on the Odyssey could not be resolved at all. However, considering that most soft tissue sarcomas are larger than the largest inclusion diameter tested here (17 mm) and that contrast ratios ≥3 would be achieved, this limitation is likely inconsequential in the clinical context.

In a previous study using surgical dissection phantoms with background tissue conditions set at 1% blood and 1% intralipid, we were able to successfully dissect inclusions with ∼1-cm margins with IBRs down to 3:1.[51] However, we were unsuccessful in dissecting the 2:1 IBR condition without cutting into the inclusion. The reason for this is likely twofold: (1) as determined in the present study, the 1% blood and 1% intralipid condition has the highest observed fluorescence among the connective tissues, which would reduce contrast, and (2) the blinded surgeon did not have a predetermined target fluorescence value as a stopping criteria. In this study, we advanced our previous techniques using surgical testing phantoms to determine both the target fluorescence value that would allow a surgeon to achieve a 1-cm margin and by accounting for the effect of volume on observed fluorescence. The volume effects are clinically relevant and especially important for the surgeon, because the fluorescence intensity increases exponentially as the surgeon cuts toward the inclusion (reducing margin depth and overall phantom volume). However, once the desired fluorescence value is achieved in the ROI, reducing the volume from the sides of the phantom caused up to a 40% and 50% reduction in the observed fluorescence value for fat and muscle, respectively. Thus, the surgeon must strategize their incisions to account for the interplay between margin thickness and overall tissue volume to achieve the desired margin.

Here, we demonstrated that a surgeon blinded to the location of the inclusion was able to accurately dissect the fluorescent inclusion with ∼1-cm margins in both fat and muscle phantom conditions and at all contrast ratios by knowing only the predetermined fluorescence value for our desired margin thickness. The largest spreads in achieved margin thicknesses were in the 5:1 to 2:1 contrast conditions. Conversely, the largest spreads in final fluorescence intensities were in the infinite and 10:1 IBR cases. This is likely due to the exponential fashion in which light is attenuated as it travels through tissue. In higher contrast cases, removing small amounts of tissue resulted in large changes in fluorescence, whereas the opposite is true for lower contrast cases. When there is less contrast, large amounts of tissue need to be removed to observe a substantial increase in fluorescence, making a consistent and accurate dissection more difficult. These data indicate the importance of determining tumor fluorophore uptake and binding prior to surgery, to account for tumor contrast while performing surgical resection.

The inability to accurately resolve target structures at low tumor-to-background ratios (TBR) is a concern for FGS, especially in the case of WLE where the goal is to remove tumor bulk and achieve a tumor-free margin simultaneously. Human trials have been performed using a single-fluorescent-targeted antibody (cetuximab-IRDye 800CW) for resection using FGS of head and neck squamous cell carcinomas.[9] Although this first-in-human study demonstrated modest TBRs (∼4.3), antibody-based FGS suffers, in general, from long injection-to-resection times on the order of days. This is thought to be the result of a complex combination of very slow plasma

clearance (hours to days), receptor binding and cellular internalization, vascular density and perfusion, and inhibited lymphatic clearance.[9] To overcome the limitation of suboptimal contrast, "cold doses" (subtherapeutic dose of naïve antibody) administered prior to the imaging antibody were investigated to deplete endogenous receptor "sinks" and increase contrast, although this was met with limited further enhancement (TBR ∼5.5).[39] The present study validates that any TBR ≥ 2 is sufficient to achieve desired margins when prior knowledge of the inclusion is known. However, using a small, targeted molecule, such as ABY-029, which will clear from the vasculature at a faster rate (minutes to hours)[25] will ultimately reduce the administration-to-resection times, increase tumor contrast, and improved the accuracy of margin assessment.

## 5 Conclusions

FGS is a promising tool for surgical resection of many cancers; however, resection of subsurface tumors is not currently amenable to the conventional direct fluorescence visualization techniques. This study validates our ability to use indirect, subsurface fluorescence measures to successfully resect a tumor-mimicking inclusion to a predetermined margin thickness using predicted fluorescence readings specific for the surgical instrument of choice. Further studies using light modeling to combine prior knowledge of tissue characteristics (background tissue optical properties, tissue pharmacokinetics, tumor size/shape/volume, and tumor EGFR concentration/expression) could be used to predict target fluorescence values equivalent to a desired margin thickness on a patient-to-patient basis. Additionally, maximizing the tumor-to-background tissue contrast ratios by carefully selecting the imaging agent and administration-to-imaging times will improve accuracy and repeatability of obtaining a clear margin of known thickness.

### References

1. K. E. Tipirneni et al., "Oncologic procedures amenable to fluorescence-guided surgery," *Ann. Surg.* **266**, 36–47 (2017).
2. W. Stummer et al., "Fluorescence-guided surgery with 5-aminolevulinic acid for resection of malignant glioma: a randomised controlled multicentre phase III trial," *Lancet Oncol.* **7**, 392–401 (2006).
3. P. A. Valdés et al., "Quantitative fluorescence in intracranial tumor: implications for ALA-induced PpIX as an intraoperative biomarker," *J. Neurosurg.* **115**, 11–17 (2011).
4. A. Mansouri et al., "The role of 5-aminolevulinic acid in enhancing surgery for high-grade glioma, its current boundaries, and future perspectives: a systematic review," *Cancer* **122**, 2469–2478 (2016).
5. P. V. Butte et al., "Near-infrared imaging of brain tumors using the Tumor Paint BLZ-100 to achieve near-complete resection of brain tumors," *Neurosurg. Focus* **36**, E1 (2014).
6. Y. Pan et al., "Endoscopic molecular imaging of human bladder cancer using a CD47 antibody," *Sci. Transl. Med.* **6**, 260ra148 (2014).
7. A. Stenzl et al., "Hexaminolevulinate-guided fluorescence cystoscopy reduces recurrence in patients with nonmuscle invasive bladder cancer," *J. Urol.* **184**, 1907–1914 (2010).

8. H. B. Grossman et al., "Long-term decrease in bladder cancer recurrence with hexaminolevulinate enabled fluorescence cystoscopy," *J. Urol.* **188**, 58–62 (2012).

9. E. L. Rosenthal et al., "Safety and tumor specificity of cetuximab-IRDye800 for surgical navigation in head and neck cancer," *Clin. Cancer Res.* **21**, 3658–3666 (2015).

10. I. Atallah et al., "Role of near-infrared fluorescence imaging in head and neck cancer surgery: from animal models to humans," *Eur. Arch. Otorhinolaryngol.* **272**, 2593–2600 (2015).

11. B. K. Potter et al., "Impact of margin status and local recurrence on soft-tissue sarcoma outcomes," *J. Bone Joint Surg. Am.* **95**, e151 (2013).

12. A. Stojadinovic et al., "Analysis of the prognostic significance of microscopic margins in 2,084 localized primary adult soft tissue sarcomas," *Ann. Surg.* **235**, 424–434 (2002).

13. P. W. Pisters et al., "Analysis of prognostic factors in 1,041 patients with localized soft tissue sarcomas of the extremities," *J. Clin. Oncol.* **14**, 1679–1689 (1996).

14. J. M. Stahl et al., "The effect of microscopic margin status on survival in adult retroperitoneal soft tissue sarcomas," *Eur. J. Surg. Oncol.* **43**, 168–174 (2017).

15. J. Fidel et al., "Preclinical validation of the utility of BLZ-100 in providing fluorescence contrast for imaging spontaneous solid tumors," *Cancer Res.* **75**, 4283–4291 (2015).

16. J. Parrish-Novak et al., "Nonclinical profile of BLZ-100, a tumor-targeting fluorescent imaging agent," *Int. J. Toxicol.* **36**, 104–112 (2017).

17. J. P. Gleysteen et al., "Fluorescent labeled anti-EGFR antibody for identification of regional and distant metastasis in a preclinical xenograft model," *Head Neck* **30**, 782–789 (2008).

18. C. H. Heath et al., "Use of panitumumab-IRDye800 to image microscopic head and neck cancer in an orthotopic surgical model," *Ann. Surg. Oncol.* **19**, 3879–3887 (2012).

19. K. E. Day et al., "Preclinical comparison of near-infrared-labeled cetuximab and panitumumab for optical imaging of head and neck squamous cell carcinoma," *Mol. Imaging Biol.* **15**, 722–729 (2013).

20. J. K. Mito et al., "Intraoperative detection and removal of microscopic residual sarcoma using wide-field imaging," *Cancer* **118**, 5320–5330 (2012).

21. M. J. Whitley et al., "A mouse-human phase 1 co-clinical trial of a protease-activated fluorescent probe for imaging cancer," *Sci. Transl. Med.* **8**, 320ra4 (2016).

22. S. Yano et al., "Targeting tumors with a killer-reporter adenovirus for curative fluorescence-guided surgery of soft-tissue sarcoma," *Oncotarget* **6**, 13133–13148 (2015).

23. S. Yano et al., "Eradication of osteosarcoma by fluorescence-guided surgery with tumor labeling by a killer-reporter adenovirus," *J. Orthop. Res.* **34**, 836–844 (2016).

24. M. V. Marshall et al., "Single-dose intravenous toxicity study of IRDye 800CW in Sprague-Dawley rats," *Mol. Imaging Biol.* **12**, 583–594 (2010).

25. K. S. Samkoe et al., "Toxicity and pharmacokinetic profile for single-dose injection of ABY-029: a fluorescent anti-EGFR synthetic affibody molecule for human use," *Mol. Imaging Biol.* **19**, 512–521 (2017).

26. B. W. Pogue et al., "Advancing molecular-guided surgery through probe development and testing in a moderate cost evaluation pipeline," *Proc. SPIE* **9311**, 931112 (2015).

27. K. Sexton et al., "Fluorescent affibody peptide penetration in glioma margin is superior to full antibody," *PLoS One* **8**, e60390 (2013).

28. A. L. R. de Souza et al., "Fluorescent affibody molecule administered in vivo at a microdose level labels EGFR expressing glioma tumor regions," *Mol. Imaging Biol.* **19**, 41–48 (2017).

29. S. C. Davis et al., "Dynamic dual-tracer MRI-guided fluorescence tomography to quantify receptor density in vivo," *Proc. Natl. Acad. Sci. U. S. A.* **110**, 9025–9030 (2013).

30. S. C. Davis et al., "Topical dual-stain difference imaging for rapid intra-operative tumor identification in fresh specimens," *Opt. Lett.* **38**, 5184–5187 (2013).

31. K. S. Samkoe et al., "Quantitative in vivo immunohistochemistry of epidermal growth factor receptor using a receptor concentration imaging approach," *Cancer Res.* **74**, 7465–7474 (2014).

32. K. M. Tichauer et al., "In vivo quantification of tumor receptor binding potential with dual-reporter molecular imaging," *Mol. Imaging Biol.* **14**, 584–592 (2012).

33. D. Keizman et al., "Expression and significance of EGFR in malignant peripheral nerve sheath tumor," *J. Neuro-Oncol.* **94**, 383–388 (2009).

34. H.-W. Teng et al., "Prevalence and prognostic influence of genomic changes of EGFR pathway markers in synovial sarcoma," *J. Surg. Oncol.* **103**, 773–781 (2011).

35. J.-L. Yang et al., "Significance of phosphorylated epidermal growth factor receptor and its signal transducers in human soft tissue sarcoma," *Int. J. Mol. Sci.* **18**, 1159 (2017).

36. J. L. Yang et al., "Expression of HER1/EGFR protein in human soft tissue sarcomas," *Eur. J. Surg. Oncol.* **32**, 466–468 (2006).

37. O. Sato et al., "Expression of epidermal growth factor receptor, ERBB2 and KIT in adult soft tissue sarcomas: a clinicopathologic study of 281 cases," *Cancer* **103**, 1881–1890 (2005).

38. A. V. DSouza et al., "Review of fluorescence guided surgery systems: identification of key performance capabilities beyond indocyanine green imaging," *J. Biomed. Opt.* **21**, 080901 (2016).

39. L. S. Moore et al., "Effects of an unlabeled loading dose on tumor-specific uptake of a fluorescently labeled antibody for optical surgical navigation," *Mol. Imaging Biol.* **19**, 610–616 (2017).

40. S. L. Jacques, "Optical properties of biological tissues: a review," *Phys. Med. Biol.* **58**, R37–R61 (2013).

41. B. Brooksby et al., "Imaging breast adipose and fibroglandular tissue molecular signatures by using hybrid MRI-guided near-infrared spectral tomography," *Proc. Natl. Acad. Sci. U. S. A.* **103**, 8828–8833 (2006).

42. H. J. van Staveren et al., "Light scattering in intralipid-10% in the wavelength range of 400–1100 nm," *Appl. Opt.* **30**, 4507–4514 (1991).

43. J. Schindelin et al., "Fiji: an open-source platform for biological-image analysis," *Nat. Methods* **9**, 676–682 (2012).

44. C. A. Schneider, W. S. Rasband, and K. W. Eliceiri, "NIH image to ImageJ: 25 years of image analysis," *Nat. Methods* **9**, 671–675 (2012).

45. J. Schindelin et al., "The ImageJ ecosystem: an open platform for biomedical image analysis," *Mol. Reprod. Dev.* **82**, 518–529 (2015).

46. A. V. DSouza et al., "Nodal lymph flow quantified with afferent vessel input function allows differentiation between normal and cancer-bearing nodes," *Biomed. Opt. Express* **6**, 1304–1317 (2015).

47. J. T. Elliott et al., "Microdose fluorescence imaging of ABY-029 on an operating microscope adapted by custom illumination and imaging modules," *Biomed. Opt. Express* **7**, 3280–3288 (2016).

48. K. S. Samkoe et al., "High vascular delivery of EGF, but low receptor binding rate is observed in AsPC-1 tumors as compared to normal pancreas," *Mol. Imaging Biol.* **14**, 472–479 (2012).

49. K. M. Tichauer et al., "Microscopic lymph node tumor burden quantified by macroscopic dual-tracer molecular imaging," *Nat. Med.* **20**, 1348–1353 (2014).

50. B. W. Pogue et al., "Fluorescence imaging in vivo: raster scanned point-source imaging provides more accurate quantification than broad beam geometries," *Technol. Cancer Res. Treat.* **3**, 15–21 (2004).

51. K. S. Samkoe et al., "Application of fluorescence-guided surgery to subsurface cancers requiring wide local excision: literature review and novel developments toward indirect visualization," *Cancer Control* 1–20 (accepted) (2017).

**Kimberley S. Samkoe** is an assistant research professor in the Department of Surgery, Dartmouth Medical School, and holds a PhD in biophysical chemistry from the University of Calgary, Canada. She has particular interest in fluorescence imaging with applications for cancer diagnosis and therapy monitoring, including *in vivo* quantification of protein receptors, photodynamic therapy, and contrast-enhanced image guidance for dosimetry and therapeutic response of solid tumors.

**Brent D. Bates** is a medical student at the Geisel School of Medicine, Dartmouth College. He received his MSc degree from the University of Toronto, Canada, where his research focused on the use of stem cell therapies for enhancing fracture and bone defect repair. He has a particular interest in therapeutics and imaging modalities for improving outcomes in orthopaedic surgery.

**Niki N. Tselepidakis** is an undergraduate student at the Whiting School of Engineering, Johns Hopkins University. She is majoring in biomedical engineering with a focus area in medical imaging, as

well as minoring in mathematics and Spanish. Upon graduation, she plans to attend medical school and continue research in the field of medical optics.

**Alisha V. DSouza** is a postdoctoral research associate at the Thayer School of Engineering, Dartmouth College. She received her PhD in engineering sciences from Dartmouth, where she worked in Professor Brian Pogue's lab in the area of fluorescence imaging and tomography for noninvasive metastasis sensing. Prior to her PhD, she received her bachelor of engineering degree in electronics and communication from Manipal Institute of Technology, India.

**Jason R. Gunn** is the life science manager of the optics in Medicine Laboratory, Dartmouth College, funded through the Thayer School of Engineering and housed within the Surgical Research Labs at the Dartmouth-Hitchcock Medical Center. His expertise is in laboratory methods for therapeutic and imaging evaluation for pancreatic cancer, glioblastoma, and xenograft models.

**Dipak B. Ramkumar** is a third-year resident in orthopaedic surgery at Dartmouth-Hitchcock Medical Center and a graduate from the Geisel School of Medicine, Dartmouth College. He plans to pursue a career in orthopaedic oncology and is currently funded by a grant from the Orthopaedic Research and Education Foundation. He has a background in biomedical physics and has a keen interest in applying this skill set to improve applications of fluorescence guidance for oncologic surgery.

**Keith D. Paulsen** is currently the Robert A. Pritzker professor of biomedical engineering at the Thayer School of Engineering at Dartmouth, professor of radiology at the Geisel School of Medicine, and director of the Advanced Imaging Center at Dartmouth-Hitchcock Medical Center. His research has focused on the development and translation of advanced imaging technology, primarily for cancer detection, diagnosis, therapy monitoring, and surgical guidance. He has authored more than 350 archival publications with an active research program, continuously funded by the National Institutes of Health for 25 years.

**Brian W. Pogue** is a professor of engineering, physics, and surgery at Dartmouth College, having a PhD from McMaster University, Canada. He works on imaging systems for surgery and radiation therapy guidance. He has published >300 peer-reviewed and >400 conference papers, on work funded by National Cancer Institute, National Institute of Biomedical Imaging and Bioengineering, and United States Department of Defense. He is on editorial boards for *Physics in Medicine and Biology*, *Medical Physics*, *Journal of Biomedical Optics*, and *Breast Cancer Research* and is an elected fellow of the Optical Society and American Institute for Medical and Biological Engineering.

**Eric R. Henderson** is an assistant professor of orthopaedic surgery at Dartmouth College. He completed medical school and an orthopedic residency at the University of South Florida and completed an orthopaedic oncology fellowship at Massachusetts General Hospital and the Rizzoli Institute, Bologna, Italy. He practices orthopaedic oncology at Dartmouth-Hitchcock Medical Center and at White River Junction VAMC.